

MOX–Report No. 11/2012

**A Patient-Specific Framework for the Analysis of the
Haemodynamics in Patients with Ventricular Assist
Device**

BONNEMAIN, J.; FAGGIANO, E.; QUARTERONI A.;
DEPARIS S.

MOX, Dipartimento di Matematica “F. Brioschi”
Politecnico di Milano, Via Bonardi 9 - 20133 Milano (Italy)

mox@mate.polimi.it

<http://mox.polimi.it>

A Patient-Specific Framework for the Analysis of the Haemodynamics in Patients with Ventricular Assist Device*

Jean Bonnemain[†], Elena Faggiano[‡], Alfio Quarteroni[‡] [†] and Simone Deparis[†]

February 9, 2012

[†] CMCS– Modeling and Scientific Computing
MATHICSE – Mathematics Institute of Computational Science and Engineering
EPFL – Ecole Polytechnique Fédérale de Lausanne
Station 8, CH-1015 Lausanne, Switzerland.
<jean.bonnemain,alfio.quarteroni,simone.deparis>@epfl.ch

[‡] MOX– Modellistica e Calcolo Scientifico
Dipartimento di Matematica “F. Brioschi”
Politecnico di Milano
via Bonardi 9, I-20133 Milano, Italy
elena.faggiano@mail.polimi.it, alfio.quarteroni@polimi.it

Keywords: Image segmentation, mesh generation, fluid-structure interaction, patient-specific, ventricular assist device.

Abstract

Nowadays ventricular assist devices play an important role in the treatment of terminal heart failure. While the devices themselves have been widely studied there are no studies of patient-specific numerical simulation in this context. This could be explained by the fact that the presence of the device induces metallic artifacts and noise in the acquired images so that conventional segmentation techniques fail. The aim of our work is to propose a robust framework for the segmentation of medical images of poor quality, the generation of high quality meshes and for the patient-specific analysis of the collected data via fluid-structure interaction (FSI) numerical simulations. First images are processed using histogram adjustment, histogram equalization, and gradient anisotropic diffusion filter. The watershed algorithm is then applied and the result is refined by the use of

*This work has been supported by the European Research Council Advanced Grant Mathematicard, Mathematical Modelling and Simulation of the Cardiovascular System Project ERC-2008-AdG 227058, and by the Swiss National Fund grant 323630-133898.

morphological operators. Then our framework allows the generation of two conforming meshes, one for the arterial lumen and the other for the arterial wall, ready for FSI simulations. We also describe the numerical model and methods used to perform FSI simulations. Final results performed on two patients demonstrate the ability of our methods: the whole strategy results suitable, robust, and accurate for patient-specific data.

1 Introduction

Mechanical circulatory support, especially ventricular assist devices (VAD), play an important role nowadays in the treatment of terminal heart failure. Initially proposed for patients who are on the transplantation waiting list (*bridge to transplantation*) [1] in the context of chronic lack of donors and raising number of patients with terminal heart failure [2] and also for patients who need a temporary support (*bridge to recovery*) [3], the indication was extended to patients who are not eligible for transplantation (*destination therapy*) [4].

While the devices themselves have been widely studied, little is known about the interaction of the machines with the cardiovascular system, especially about the geometric configuration (size, type, location) of the anastomosis between outflow cannula of the device and the aorta. It has already been shown that it plays an important role in the generation of abnormal haemodynamic pattern, both *in vivo* [5], *in vitro* [6], and *in silico* [7], [8], [9], or [10]. To further improve the knowledge about the influence of cannula configuration in the aortic haemodynamic one should consider patient-specific models of the aorta with the cannula. However, nowadays, in the VAD context there are no studies of patient-specific numerical simulations. In fact, in all the previously cited studies computational simulations are performed on a representative geometry of the human aortic arch, generated either from medical images (e.g. computed tomography (CT)) of healthy people [9], [8], [7] or from clinical measurements [10], on which the cannula is artificially added. These assumptions can be made in the case of testing different configurations for generic results, but not in the context of patient-specific numerical simulations, that are designed to model different kind of clinical situations, and also to validate the numerical results with clinical data [11]. Moreover, exception made for [8], the arterial wall is always considered rigid instead of deforming under the action of blood pressure pulse.

The lack of patient-specific simulations is mainly explained by the fact that the presence of the device induces metallic artifacts and noise in the acquired images (usually CT-scan [12], [13]) so that conventional segmentation techniques fail, generating aberrant geometries.

Besides, the whole process from medical images acquisition to numerical simulations is characterized by the following steps: (1) segmentation, (2) generation of suitable surfacic and volumic meshes, and (3) perform meaningful and relevant CFD simulations, remains a challenge and is time consuming, even more with images of poor quality as in VAD case. Whereas already existing frame-

work are available [14], [15] they do not provide automatic tools to deal with noisy images, and are not suitable to generate meshes that are appropriate for simulate fluid-structure interaction (FSI) in case like the present one, in which the different thickness and physical properties of the arterial and the cannula wall require special treatment.

The aim of this work is to develop a general framework that provides semi-automatic and robust tools to perform all the steps required for numerical simulations, starting from CT images of patients having VAD to generation of suitable meshes for FSI simulations. We also present the numerical methods and tools we use to perform such simulations and a few preliminary results of the entire process.

2 Methods

Radiological assessment of patient under mechanical circulatory support is usually performed by computed tomography [12], [13]. The same images can be used to perform patient-specific numerical simulations and deeply explore the fluid dynamic in these patients. In this study we consider two patients, Patient 1 who received a continuous flow left ventricular assist device (LVAD), and Patient 2 holding a pulsatile biventricular assistance. A CT scanner of each patient was acquired with the LightSpeed VCT model (from GE Medical Systems) for postoperative control and pulmonary embolism suspicion respectively. The acquisition protocol generates a stack of axial images with a slice thickness of 1.25 mm.

To perform patient-specific simulations the first necessary step is to obtain a good reconstruction of the patient aorta and cannula geometry. In the next session we present a semi-automatic procedure to reach this goal and correctly segment VAD patient CT images. After segmentation, a mesh generation step is required; this is very important because mesh quality could influence numerical simulation results. Moreover, for FSI simulations, conforming meshes for fluid and structure are needed with the appropriate boundary flags for the assignment of the material physical properties and the correct boundary conditions. In a second section we present our automatic tool to generate these type of high quality meshes with a maximum freedom in flags generation. As last we also present our framework to perform such FSI simulations.

The segmentation and mesh generation procedure is mainly implemented based on the libraries The Insight Segmentation and Registration Toolkit (itk) [16] [17], The Visualization Toolkit (VTK) [18] and The Vascular Modeling Toolkit (vmtk) [19]. The numerical simulations are performed using the library LifeV [20]. All the used libraries are open-source libraries implemented in C++, and cross-platform (Windows, except for LifeV, Unix, and MacOS X).

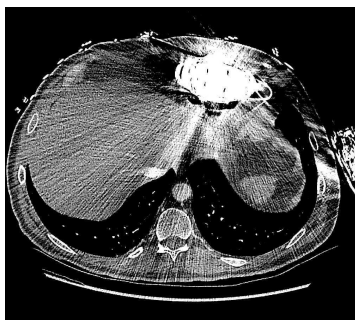


Figure 1: A slice of a CT image of Patient 1.

2.1 Segmentation

Starting from the volume of voxels containing tissue attenuation values expressed in Hounsfield Units (HU), the goal of our segmentation method is the extraction of the surface individuating the interface between blood and wall of the aorta and the VAD outflow cannula with a particular attention to the anastomosis area; on CT-scan data the arterial and cannula wall are usually not visible. Unfortunately, segmentation of these images is not trivial because of the metallic noise due to the device and the non-aortic contrast phase. An example of this type of images can be seen in figure 1 in which the noise effect due to the metallic machine and the bad and non-uniform contrast of the aorta are evident. In these situations image segmentation with standard and automatic tools is not feasible, therefore we propose an original procedure to overcome this problem and correctly segment this kind of images.

The whole procedure can be divided in three steps: pre-processing, segmentation step, and refinement.

2.1.1 Pre-processing

The first step aims at enhancing the image intensity contrast and at filtering the image noise. First of all we perform a combination of histogram adjustment and histogram equalization. The adjustment is performed trimming the image intensity values between -1000 HU and +1000 HU and performing a linear adjustment of the dynamic range for the remaining intensities. In this way we compress the metallic range in one single value (1000 HU) and we stretch the dynamic range of the tissues. Secondly the contrast-limited adaptive histogram equalization method [21] is applied. This method applies the classical concept of histogram equalization to small local areas of the image and interpolates the local result to produce a homogeneous result. The method allows the regions of the image to be enhanced differentially, i.e., we are able to enhance the contrast in the aorta excluding in the equalization the metal region; the result is an acceptable compromise between contrast enhancement and noise enhance-



Figure 2: A screenshot of one slice of the result of watershed algorithm. Different grey levels represent different regions individuated by the algorithm. Ca: cannula, AscAo: ascending aorta, DescAo: descending aorta.

ment. The method is applied slice-by-slice with a window size of 64×64 pixels and a clipping level of 57 pixel per bin. In the following we call the histogram adjustment plus histogram equalization the histogram enhancement filter.

We then apply a gradient anisotropic diffusion filter, which allows to remove the noise from homogeneous regions while keeping clear and sharp edges [22]. In fact this filter performs a smoothing which is less pronounced at edges measured as high gradient magnitude. The parameters controlling this filter are the *conductance* and the *iteration* [17]. The lower the conductance parameter, the more strongly the diffusion equation preserves image features; the higher the iteration value, the more blurred the image will become. Typical values we use for conductance and iteration values are 1 and 5 respectively.

2.1.2 Segmentation

The core of the segmentation procedure is the segmentation itself. To segment the pre-processed image we use the watershed segmentation [23], [24], as implemented in itk [17] [25].

The watershed segmentation treats the image to segment as a height function, i.e., the pixel gray level corresponds to the altitude of a point on a surface. First a gradient filter is applied so that feature edges can be seen as ridges and uniform intensity areas as basins. The idea is to see the result of the segmentation as this virtual topography flooded by water: increasing the level of water the size of the basins grow because they merge with adjacent basins. The remaining ridges after the flooding are the image boundaries. The parameters controlling this procedure are the *threshold* and the *level* [17]. Both are set as a fraction of the maximum depth of the input image. The threshold indicates the background noise to remove before segmentation. We fixed this parameter for this study at a low value of 0.005. The level parameter allows to minimize over-segmentation

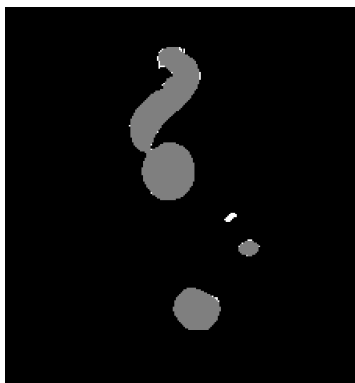


Figure 3: One slice of the segmented image after the morphological enhancement filter. In gray the final segmentation and in white the regions corrected by the filter.

controlling the level of flooding, i.e., by establishing a minimum watershed depth. Adjacent regions are merged if their combined depth falls below the minimum. Higher values of level parameter result in lower segmentations. We choose this parameter in the range $0.15 - 0.25$. Last, as watershed algorithm produces a segmentation of the entire image (see figure 2) we have implemented a graphic interface which allows to select at the end of the process the regions (basin) which represent the region of interest (i.e., the aortic arch and cannula). The image produced by this segmentation step is a binary image with value 1 inside the region of interest and zero outside.

2.1.3 Refinement

This last step relies on morphological operators [26] [27]: in particular we perform on the segmentation output image a “morphological enhancement” operation which consists in the sum of the image with the result of a “top hat” operation and the negative of the result of a “bottom hat” operation, where both “top hat” and “bottom hat” operations are performed with the same sphere structuring element with a radius chosen by the user. In our study we choose the radius in the range $1 - 3$. This procedure eliminates small holes and small features in the generated segmentation as can be seen in figure 3, where in gray is represented the final segmentation and in white the regions corrected by the morphological enhancement filter. The output image is then rescaled between 0 and 255 and then processed with a last smoothing which penalizes high curvatures and which transforms the resulting image in a level set function, i.e., an image whose zero level is the searched surface.

2.2 Mesh generation

In this section we describe the tools and methods to generate suitable grids for our finite element library LifeV [20]. Although the output of our procedure is a LifeV mesh, there is an easy way to export the mesh in different commonly used formats. This step is critical since the mesh can change the accuracy of the numerical results and the efficiency of numerical methods, e.g. the computational time or convergence. It is worthwhile to precise that in our case, the FSI model uses two conforming meshes: one for the fluid domain, i.e., the lumen, and one for the solid domain, i.e., the arterial wall and the cannula; the two meshes are conforming at the interface. As explained in Section 2.1, the segmentation procedure only allows to recover the interface between the blood and the arterial wall, the arterial wall itself being usually not seen on CT-scan data. Fluid and solid domain meshes must be created starting from the recovered interface. The fluid domain mesh is easy to generate since it is the space inside the interface surface. The arterial wall instead needs to be synthetically reconstructed; later on we describe this procedure. Our mesh generation procedure consists in three steps: creation of a surface mesh, smoothing of the initial surface mesh, and creation of the final fluid and solid meshes.

2.2.1 Creation of a surface mesh

As described in section 2.1, the last data obtained by the segmentation procedure is a set of images of which the zero level is the surface of interest. To recover the polygonal surface mesh (i.e., a triangulation of the zero level image) we use the marching cubes algorithm [28] as implemented in vmtk; this step does not require user interaction and is therefore completely automatic.

2.2.2 Smoothing the surfaces

A known drawback of the marching cubes method is the resulting staircase effect on the surface related to the discrete nature of the data [29]. To remove this surface aliasing we first apply Gaussian filters using Freeyams [30] [31], [32]. The residual artifacts on the surface are then removed using the Taubin algorithm [33] implemented in VTK. These two steps are semi-automatic since they only need few parameters: the number of iterations for the Taubin algorithm and the Gaussian filters and the pass band for the Taubin algorithm. For our tests we used a number of iterations equal to 1000 and 40 for Gaussian and Taubin filters, respectively, and a pass band of 0.001 for the Taubin filter.

2.2.3 Final meshes

For the generation of the final tetrahedral meshes we implemented a semi-automatic Python code based on the VTK and vmtk libraries. The input is the surface mesh and the output is the fluid and the solid tetrahedral meshes.

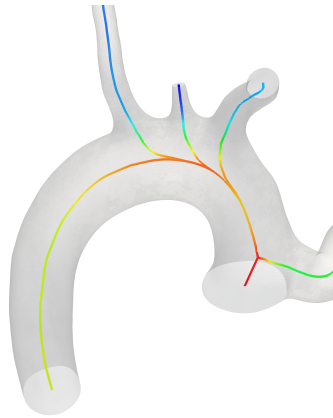


Figure 4: Centerlines.

During execution only relevant parameters are interactively asked to the user, making it easy to use and understand.

The principle is to further improve the quality of the surface mesh and then use it as a basis for the fluid mesh, which is generated filling the volume with tetrahedra, and for the solid mesh, which is generated extruding the surface mesh along surface normals. As preliminary remark, it is important to underline that this framework mainly relies on the centerlines computation [34] available in vmtk, which in turn gives the possibility to calculate the distance between centerlines and surface mesh, which corresponds to local vessel size. Mesh elements area (triangles or tetrahedra) is eventually computed in function of the local diameter, avoiding over refinement of large structure (e.g. the aorta) and providing a mesh fine enough for small vessels (e.g. coronary artery). Fig. 4 shows the result of centerlines computation on the surface mesh obtained after the application of the Taubin filter. The description of the different steps follows.

- (a) *Surface remeshing*: First centerlines are computed on the initial surface mesh obtained in section 2.2.2. Then it is remeshed in function of a given constant factor making the triangle area proportional to the local size of the vessel [34].
- (b) *Fluid meshing*: The newly optimized surface mesh is filled with tetrahedra. The volume size of the elements is set proportionally to the length of edges of the surface triangles. The user also has the possibility to add a boundary layer, specifying various parameters as the number of sublayers and the thickness of each sublayer. Finally the mesh can be scaled to the convenient units, in our case centimeters, and the flags are automatically added to the boundaries.
- (c) *Solid meshing*: The solid mesh is created by extruding the surface mesh toward the normal direction, the thickness given by a proportionality factor

of the local vessel size or by a constant factor. The user can interactively define multiple regions on the surface mesh and apply the previously described method. Therefore for each of these areas it is possible (i) to give a specific thickness to the solid mesh, constant or vessel radius dependent, and (ii) to automatically give different surface flags to the external surface (triangles) of the solid mesh and also different volumetric flags to the tetrahedra of this area.

Points (a) and (b) are available commands in vmtk, whereas point (c) was specifically developed.

2.3 Numerical simulations

We are interested in simulating blood flow in vascular districts. The arteries are compliant vessels that react to mechanical and chemical signals. These aspects can be partially taken care by defining appropriate constitutive laws. Which one is the most appropriate, is still an open question. In most of the cases, we can not avoid to consider the mechanical interaction and we have to consider the fully coupled blood-flow / vessel wall system. Our model therefore includes two media, the fluid and the structure, and interaction at the mechanical level, which is governed by coupling conditions expressing the continuity of the velocities and the equilibrium of the structure. The model expresses Fluid-Structure Interaction (FSI), whose solution needs specific coupling algorithms.

We start by identifying a fluid and a structure computational domains, Ω_f and Ω_s respectively, thanks to the segmentation and mesh generation previously described. We define a fluid-structure interface Γ_{FSI} as $\partial\Omega_f \cap \partial\Omega_s$, which is the region where the mechanical coupling takes place. The equations governing the structure are described in a Lagrangian frame of reference, meaning that we only need a fixed computational domain. The blood flow is described by the Navier-Stokes equations in a moving domain and we are interested in a specific region, the segmented piece of artery. In this situation it is appropriate to describe the equations in an Arbitrary Lagrangian-Eulerian (ALE) frame of reference. This means that the fluid computational domain $\Omega_f(t)$ is time dependent and its movement is described by an ALE mapping

$$\begin{aligned} \mathcal{A}_t : \Omega_f &\rightarrow \Omega_f(t) \\ \mathbf{x} &\rightarrow \mathcal{A}_t(\mathbf{x}) = \mathbf{x} + \mathbf{d}_f(x), \end{aligned}$$

where \mathbf{d}_f is the displacement of the fluid domain. In particular $\Omega_f(t) = \mathcal{A}_t(\Omega_f, t)$. This choice generates an additional coupling condition, called geometry adherence, that guarantees that the fluid and structure domains adhere to each other. In other words, $\mathbf{d}_f = Ext(\mathbf{d}_s|_{\Gamma_{FSI}})$, where \mathbf{d}_s is the solid displacement and the extension $Ext(\cdot)$ operator, e.g. an harmonic lifting (or extension), from Γ_{FSI} to Ω_f (see [35]).

With the definition of a particular structural constitutive law through its first Piola-Kirchhoff stress tensor $\mathbf{\Pi} = \mathbf{\Pi}(\mathbf{d}_s)$ — here we use linear elasticity — the structure equation with unknown \mathbf{d}_s reads

$$\rho_s \partial_{tt} \mathbf{d}_s - \nabla \cdot \mathbf{\Pi} = 0 \quad \text{in } \Omega_s,$$

where ∂_{tt} is the second partial derivative with respect to time. Thanks to the ALE mapping and the definition of the fluid domain velocity $\mathbf{w} = \mathbf{w}(\mathbf{x}, t) = \partial_t \mathbf{d}_f$ we can formulate the Navier–Stokes equations in the ALE form as

$$\begin{cases} \rho_f \partial_t \mathbf{u} + \rho_f (\mathbf{u} - \mathbf{w}) \cdot \nabla \mathbf{u} - \nabla \cdot \sigma_f & = 0 & \text{in } \Omega_f(t) \\ \nabla \cdot \mathbf{u} & = 0 & \text{in } \Omega_f(t). \end{cases}$$

Here $\mathbf{u} = \mathbf{u}(\mathbf{x}, t)$ is the fluid velocity, $p = p(\mathbf{x}, t)$ the pressure, ∂_t the partial derivative with respect to the time, ρ_f and ρ_s the fluid and solid densities, $\sigma_f = \sigma_f(\mathbf{u}, p) = -p\mathbf{I} + \mu\epsilon(\mathbf{u})$ the fluid Cauchy stress tensor, μ the fluid dynamic viscosity, and $\epsilon(\mathbf{u}) = (\nabla \mathbf{u} + \nabla \mathbf{u}^T)/2$ the strain rate tensor. $\mathbf{F}_f = \nabla \mathcal{A}_t$ is the fluid domain gradient of deformation, $J_f = \det \mathbf{F}_f$ the Jacobian, \mathbf{n}_f and \mathbf{n}_s the outward unit normals to the fluid and solid domains.

The coupling conditions at the fluid-structure interface, the continuity of the velocity, the equilibrium of the stresses, and the geometric adherence, are summarized as follow:

$$\begin{cases} \mathbf{u} \circ \mathcal{A}_t = \partial_t \mathbf{d}_s & \text{on } \Gamma_{FSI}(t), \\ \mathbf{\Pi} \mathbf{n}_s = -J_f \sigma_f \circ \mathcal{A}_t (\mathbf{F}_f)^{-T} \mathbf{n}_f \circ \mathcal{A}_t & \text{on } \Gamma_{FSI}, \\ \mathbf{d}_f = \mathbf{d}_s & \text{on } \Gamma_{FSI}. \end{cases}$$

Additional conditions on the external boundary are necessary to close the system. The tissue surrounding the artery can be mimicked by Robin boundary conditions (e.g. [36]). It is more difficult to assign the correct flow conditions upstream and downstream of the fluid domain. If the data on the flowrates is available, e.g. [37], then it is possible to assign these values by ad-hoc Lagrange multipliers [38]. Otherwise it is necessary to have a rough description of the whole cardiovascular system, e.g., by a network of one-dimensional models [39, 40, 41, 42]. We use this multiscale description in our simulations.

The equations are first written in a weak form, discretized in time and finally in space, cf. [43]. To discretize the problem in time we use a geometry-convective explicit (GCE) time advancing scheme. This scheme, besides being stable, has the main advantage to reduce the spatial discrete problem to a linear problem. The other terms are treated using a first order backward Euler scheme. We consider all the state variables of the coupled problem — structure displacement, fluid velocity, pressure, and domain displacement — as a single unknown. We use P1 finite elements for each state variable and we stabilize the saddle-point problem by interior penalty [44]. The linear system is solved in parallel using

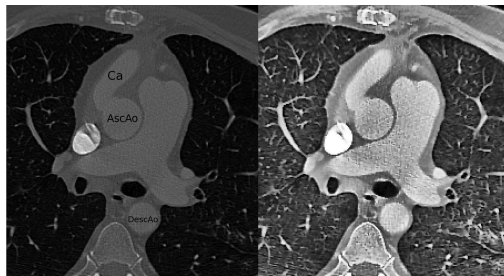


Figure 5: Left: A slice of CT-scan of Patient 1. AscAo: ascending aorta, DescAo: descending aorta, Ca: cannula. Right: after the pre-processing step i.e. gradient anisotropic diffusion filter added to the histogram enhancement filter.

GMRES iterations and overlapping algebraic Schwarz preconditioners based on an inexact block factorization of the system (see [36]). The software used in the simulations is based on LifeV [20].

3 Results and Discussion

In this section we present the results of our investigations for the two set of images of the patients mentioned before. For reason of convenience we display the pictures for each step for Patient 1 whereas we show only a few images for Patient 2.

3.1 Segmentation

A significant slice of the CT of Patient 1 is shown in fig. 5 (left): in this slice the aortic arch with the anastomosis and the VAD outflow cannula are evident.

The image is characterized by the VAD device noise and the aorta and cannula are not well contrasted.

Fig. 5 (right) represents the same slice after the pre-processing step i.e. after the histogram enhancement filter plus the gradient anisotropic diffusion filter. At the end of the pre-processing step the contrast of the aorta and cannula is clearly improved and the noise due to the device decreased.

To numerically verify this improvement we calculated the contrast-to-noise ratio (CNR) on the original image (CT), on the image treated with the histogram enhancement filter (CT-HEF) and on the result of the previous step plus the gradient anisotropic diffusion filter (CT-GADF). A representative region of interest (ROI) was taken including a portion of both the aortic arch and the cannula; the same region was considered in the three compared images (CT, CT-HEF and CT-GADF) for each patient. A second region representative of the background (bkg) was chosen near the aorta to evaluate the contrast between

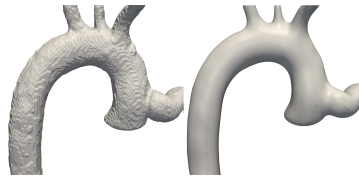


Figure 6: Polygonal surface mesh: result of the marching cube method (left), same mesh after the smoothing by Gaussian and Taubin filters (right). Posterior views.

aorta and adjacent structures. CNR was then calculated as:

$$CNR = \frac{contrast}{noise} = \frac{(\mu_{ROI} - \mu_{bkg})}{\sqrt{(\sigma_{ROI}^2 + \sigma_{bkg}^2)}/2}$$

where μ_{ROI} is the mean of the image intensity values in the ROI and μ_{bkg} is the mean of the intensity values in the bkg; σ_{ROI} and σ_{bkg} are the standard deviations of image intensities in the ROI and bkg respectively. CNR is a measure used to determine image quality and is higher for better quality images.

Table 1: Contrast-to-noise ratio (CNR) of the original image (CT-original), after the application of the histogram enhancement filter (CT-HEF) and after the application of the gradient anisotropic diffusion filter (CT-GADF), for patients 1 and 2.

	CT-original	CT-HEF	CT-GADF
Patient 1	3.4503	4.5574	12.3662
Patient 2	7.7783	8.7904	16.2073

In table 1 are reported the CNR values calculated for patients 1 and 2: in both cases the CNR value increase with the application of the histogram enhancement filter and increase even more with the addition of the second filter.

For both patients after the pre-processing step the watershed algorithm succeeded in the segmentation of the aortic arch and cannula. The refinement step has always proved necessary to remove the noise captured by the watershed algorithm i.e. holes and small isolated features.

3.2 Mesh generation

In this section we show the results obtained using the framework presented in section 2.2. Fig. 6 (left) shows the result of the marching cubes algorithm applied to data obtained by segmentation. One can clearly see the staircase effect, being removed by applying the Gaussian filters and Taubin algorithm (fig. 6 (right)).

In particular in Fig. 7 we show a detail of the three meshes (marching cubes, Gaussian and Taubin): the Gaussian filters implemented in Freeyams well succeed in the correction of the staircase effect but introduce some artifacts (evident



Figure 7: Polygonal surface mesh: result of the marching cube method (left), Gaussian filters (center), and Taubin algorithm (right). Posterior views.

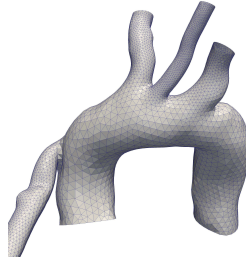


Figure 8: Final surface mesh of Patient 2. Anterior view.

in fig. 7, center). All these artifacts are completely removed by the Taubin filter. The generated surface is sufficiently smooth without being shrunk and the final meshes can be generated. In fig. 8 we report the final mesh also for Patient 2.

Thanks to our implemented framework we create the mesh of the cannula with a constant thickness (given by manufacturer), and generate the arterial wall with a thickness proportional to the local vessel size [45]. Also we choose two different flag values for both the surface and volume of these two regions, giving the opportunity to provide different sets of boundary conditions and to apply different Young moduli, respectively. Moreover we separately define multiple areas for all the different vascular branches (e.g. ascending aorta, carotid artery, subclavian artery) in order to apply different set of Robin boundary conditions on the external surface of the arterial wall. This allows to model in a more accurate way the physical properties of the arterial tree [36], [46].

Fig. 9 shows the final surface mesh for Patient 1 with the selection of a specific area (the outflow cannula of VAD) and the multiple regions to which different physical properties can be applied thanks to the flags attribution.

Finally fig. 10 displays the fluid mesh. One can remark the refinement of tetrahedra in function of the diameter of the local radius. Fig. 11 depicts the solid mesh. The thickness of the structure is proportional to the local radius for the aorta and its branches, and constant for the outflow cannula of the device.

3.3 Simulations

The methodological infrastructure described before allows to consider many different specific situations. The mesh of the cannula has a special flag, allowing

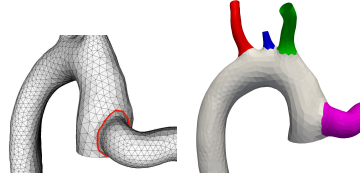


Figure 9: Left: Selection of specific areas. Right: Result of the surface flags attribution. Postero-lateral and posterior views.

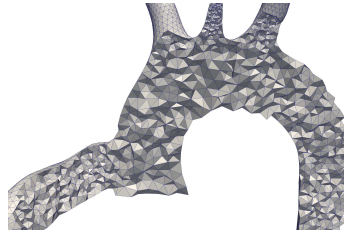


Figure 10: Fluid mesh, Patient 1. Anterior view.

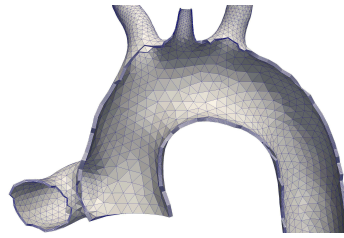


Figure 11: Solid mesh, Patient 1. Anterior view.

for a different Young modulus in the simulation settings. The model has been coupled to a geometry multiscale network that takes into account mean flow quantities of the whole arterial tree [46]. The total flow rate at the aortic root is set equal to zero; note on Fig. 12 the velocity is not equal to zero there. The flow rate at the cannula is imposed to be equal to the usual flow-rate of a healthy left ventricle. Future work includes the development of more accurate inflow conditions, e.g. including both pulsatile and continuous flow rates or the case where the left ventricle is also contributing to the flow.

We present preliminary results obtained with the case of Patient 1 showing the possible applications of the presented workflow. The fluid and structure meshes have 194'095 and 197'412 tetrahedra respectively. The total degrees of freedom is 291'527, i.e., 4 times the number of vertices in the fluid mesh, 3 times those in the structure mesh, and 3 times those on the fluid-structure interface. The time step chosen is 0.001 second. The simulation of one heart beat took 22 hours using 64 cores on an IBM Intel Nehalem cluster composed by blades containing two quad-core (Intel Nehalem 2.66 GHz) nodes each.

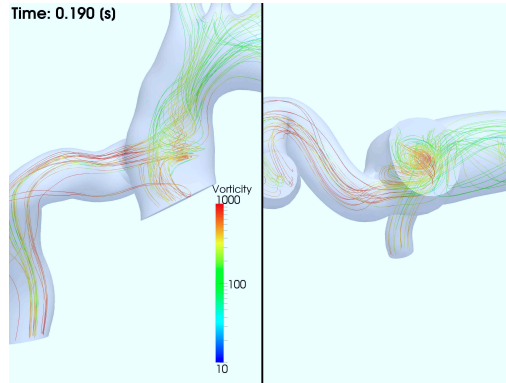


Figure 12: Vorticity patterns [s^{-1}] in the ascending aorta during systole. Anterior and inferior views.

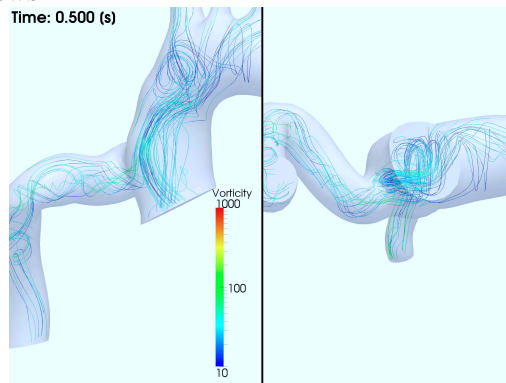


Figure 13: Vorticity patterns [s^{-1}] in the ascending aorta during systole. Anterior and inferior views.

The fluid density is set to 1.04 g/cm^3 , the fluid viscosity 0.035 g/cm/s , the Poisson coefficient 0.48, the Young modulus of the cannula $1.0784 \cdot 10^7 \text{ g/cm/s}^2$, the one of the arterial wall $3.0784 \cdot 10^6 \text{ g/cm/s}^2$. The flow near the anastomosis shows a complex behavior, we see that during the systolic phase there are vorticity patterns forming in the ascending aorta, cf. Fig. 12, while they disappear during diastole, cf. Fig. 13. The displacement of the vessel wall is not uniformly distributed (Fig. 14). Fig. 15 show the wall shear stress (WSS) on the aorta during systole. WSS is very important since its distribution on the arterial wall can have short term negative effects (e.g. thrombus formation) while in the long-term has an impact on arterial remodeling and atherosclerosis. For this specific case, WSS is particularly interesting near the anastomosis and in the aortic wall, in front of the outflow tract of the VAD: WSS is high and could lead to short and long term dysfunctions. The high WSS on the right common carotid is not correct due to the inaccurate imposition of the Robin boundary conditions accounting for the surrounding tissue.

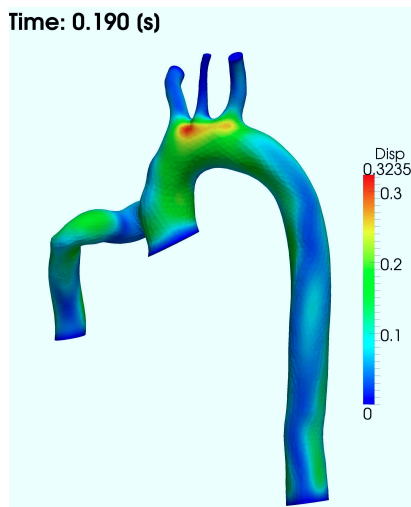


Figure 14: Displacement [cm] of the vessel wall during systole. Anterior view.

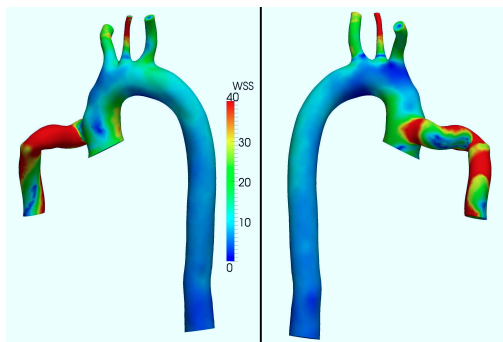


Figure 15: WSS patterns [dyn/cm^2] during systole. Anterior and posterior views.

4 Conclusion

In this work we have presented a framework for the segmentation of medical images of poor quality, the generation of high quality meshes and for the patient-specific analysis of the collected data via FSI numerical simulations. We have developed these methods specifically for the case of the anastomosis of outflow cannula of VAD to the aorta, but the method could be applied to the case of right ventricle assistance, or in a more general context. In this precise field medical images are unfortunately most of the time of poor quality due to the nature of the devices and the imaging modality, i.e. computed tomography. In spite of this difficulty, we believe that making patient-specific analysis in this context is nowadays important for the determination of individualised treatments. To date only few works studied numerically the region of anastomosis, even less with

patient-specific data. However the raising number of patients with mechanical circulatory support emphasizes the need of such studies.

Our new proposed strategy overcomes the low quality problem succeeding in geometry extraction and high quality mesh generation; moreover our FSI framework seems able to produce reliable results on the fluid-dynamics of these patients. The whole strategy marks therefore a first step towards a suitable, robust and accurate treatment of patient-specific data. Moreover the code we propose is semi-automatic, reduces the time needed to perform the entire procedure, and also minimizes the parameters asked to the user. It makes this framework usable by a larger public and also reduces the errors due to user manipulation.

We tested our methods successfully on CT-scan data of two patients under mechanical circulatory support.

As future work we plan to apply our framework to a large number of cases in order to provide a deep insight of flow dynamics in the region of anastomosis of the outflow cannula of ventricular assist devices and the aorta. We are also working on the boundary conditions we provide to our numerical model, more precisely by developing a lumped model of the entire cardiovascular system featuring the presence of an assist device. Finally an *in vitro* validation of the numerical simulations is ongoing in order to compare the numerical results with the experimental ones.

Acknowledgements

The authors acknowledge Professor L.K. von Segesser for his valuable help, especially in the clinical field. They also thank the entire LifeV community.

References

- [1] L. W. Miller *et al.*, “Use of a continuous-flow device in patients awaiting heart transplantation,” *The New England journal of medicine*, vol. 357, no. 9, pp. 885–896, Aug. 2007.
- [2] V. L. Roger *et al.*, “Heart disease and stroke statistics – 2011 update: A report from the american heart association,” *Circulation*, vol. 123, no. 4, pp. e18–e209, 2011.
- [3] E. J. Birks, P. D. Tansley, J. Hardy, R. S. George, C. T. Bowles, M. Burke, N. R. Banner, A. Khaghani, and M. H. Yacoub, “Left ventricular assist device and drug therapy for the reversal of heart failure.” *The New England journal of medicine*, vol. 355, no. 18, pp. 1873–1884, Nov. 2006.

- [4] E. A. Rose *et al.*, “Long-term mechanical left ventricular assistance for end-stage heart failure,” *The New England journal of medicine*, vol. 345, no. 20, pp. 1435–1443, Nov. 2001.
- [5] K. N. Litwak, S. C. Koenig, H. Tsukui, S. I. Kihara, Z. Wu, and G. M. Pantalos, “Effects of Left Ventricular Assist Device Support and Outflow Graft Location Upon Aortic Blood Flow,” *ASAIO journal*, vol. 50, no. 5, pp. 432–437, Sep. 2004.
- [6] K. N. Litwak, S. C. Koenig, R. C. Cheng, G. A. Giridharan, K. J. Gillars, and G. M. Pantalos, “Ascending aorta outflow graft location and pulsatile ventricular assist provide optimal hemodynamic support in an adult mock circulation.” *Artificial organs*, vol. 29, no. 8, pp. 629–635, Aug. 2005.
- [7] T. A. S. Kaufmann, M. Hormes, M. Laumen, D. L. Timms, T. Linde, T. Schmitz-Rode, A. Moritz, O. Dzemali, and U. Steinseifer, “The impact of aortic/subclavian outflow cannulation for cardiopulmonary bypass and cardiac support: a computational fluid dynamics study.” *Artificial organs*, vol. 33, no. 9, pp. 727–732, Sep. 2009.
- [8] Y. Bazilevs, J. R. Gohean, T. J. R. Hughes, R. D. Moser, and Y. Zhang, “Patient-specific isogeometric fluid–structure interaction analysis of thoracic aortic blood flow due to implantation of the Jarvik 2000 left ventricular assist device,” *Computer Methods in Applied Mechanics and Engineering*, vol. 198, no. 45–46, pp. 3534–3550, Sep. 2009.
- [9] A. G. Brown, Y. Shi, A. Arndt, J. Muller, P. Lawford, and D. R. Hose, “Importance of realistic LVAD profiles for assisted aortic simulations: evaluation of optimal outflow anastomosis locations,” *Computer Methods in Biomechanics and Biomedical Engineering*, Mar. 2011, first published online.
- [10] A. F. Osorio, R. Osorio, A. Ceballos, R. Tran, W. Clark, E. A. Divo, I. R. Argueta-Morales, A. J. Kassab, and W. M. DeCampli, “Computational fluid dynamics analysis of surgical adjustment of left ventricular assist device implantation to minimise stroke risk,” *Computer Methods in Biomechanics and Biomedical Engineering*, pp. 1–17, Dec. 2011.
- [11] J. Oden, T. Belytschko, I. Babuska, and T. Hughes, “Research directions in computational mechanics,” *Computer Methods in Applied Mechanics and Engineering*, vol. 192, no. 7–8, pp. 913–922, 2003.
- [12] S. V. Raman, A. Sahu, A. Z. Merchant, L. B. Louis, M. S. Firstenberg, and B. Sun, “Noninvasive assessment of left ventricular assist devices with cardiovascular computed tomography and impact on management,” *The Journal of heart and lung transplantation*, vol. 29, no. 1, pp. 79–85, Jan. 2010.

- [13] D. Acharya, S. Singh, J. A. Tallaj, W. L. Holman, J. F. George, J. K. Kirklin, and S. V. Pamboukian, "Use of Gated Cardiac Computed Tomography Angiography in the Assessment of Left Ventricular Assist Device Dysfunction," *ASAIO journal*, vol. 57, no. 1, pp. 32–37, Jan. 2011.
- [14] J. Peir, S. J. Sherwin, and S. Giordana, "Automatic reconstruction of a patient-specific high-order surface representation and its application to mesh generation for cfd calculations." *Med Biol Eng Comput*, vol. 46, no. 11, pp. 1069–83, 2008.
- [15] R. Torii and M. Oshima, "An integrated geometric modelling framework for patient-specific computational haemodynamic study on wide-ranged vascular network," *Computer Methods in Biomechanics and Biomedical Engineering*, pp. 1–11, 2011.
- [16] (2012) The insight segmentation and registration toolkit website. [Online]. Available: <http://www.itk.org>
- [17] L. Ibanez, W. Schroeder, L. Ng, and J. Cates, "The ITK software guide: the insight segmentation and registration toolkit," *Kitware Inc*, vol. 5, 2003.
- [18] (2012) The visualization toolkit website. [Online]. Available: <http://www.vtk.org>
- [19] (2012) The vascular modeling toolkit website. [Online]. Available: <http://www.vmtk.org>
- [20] (2012) Lifeste website. [Online]. Available: <http://www.lifeste.org>
- [21] K. Zuiderveld, "Contrast limited adaptive histogram equalization," in *Graphics gems IV*. Academic Press Professional, Inc., 1994, pp. 474–485.
- [22] P. Perona and J. Malik, "Scale-space and edge detection using anisotropic diffusion," *Pattern Analysis and Machine Intelligence, IEEE Transactions on*, vol. 12, no. 7, pp. 629–639, 1990.
- [23] L. Vincent and P. Soille, "Watersheds in digital spaces: An efficient algorithm based on immersion simulations," *IEEE Transactions on Pattern Analysis and Machine Intelligence*, vol. 13, pp. 583–598, 1991.
- [24] S. Beucher and F. Meyer, *The morphological approach to segmentation: the watershed transformation*. CRC Press, 1993, pp. 433–481.
- [25] A. Mangan and R. Whitaker, "Partitioning 3d surface meshes using watershed segmentation," *Visualization and Computer Graphics, IEEE Transactions on*, vol. 5, no. 4, pp. 308–321, 1999.
- [26] H. Heijmans, "Morphological image operators," *Advances in Electronics and Electron Physics Suppl., Boston: Academic Press*, vol. 1, 1994.

- [27] T. Kong and A. Rosenfeld, *Topological algorithms for digital image processing*. North Holland, 1996, vol. 19.
- [28] W. E. Lorensen and H. E. Cline, “Marching cubes: A high resolution 3d surface construction algorithm,” *Computer Graphics*, vol. 21, pp. 163–169, August 1987.
- [29] H. Theisel, “Exact isosurfaces for marching cubes,” in *Computer Graphics Forum*, vol. 21, no. 1. Wiley Online Library, 2002, pp. 19–32.
- [30] P. J. Frey, “Generation and adaptation of computational surface meshes from discrete anatomical data,” *International Journal for Numerical Methods in Engineering*, vol. 60, no. 6, pp. 1049–1074, 2004.
- [31] —, “Yams a fully automatic adaptive isotropic surface remeshing procedure,” GAMMA - INRIA Rocquencourt, Tech. Rep. RT-0252, Nov. 2001.
- [32] (2012) Freeyams. [Online]. Available: <http://www.ann.jussieu.fr/frey/software.html>
- [33] G. Taubin, “A signal processing approach to fair surface design,” in *Proceedings of the 22nd annual conference on Computer graphics and interactive techniques*, ser. SIGGRAPH '95. New York, NY, USA: ACM, 1995, pp. 351–358.
- [34] L. Antiga, M. Piccinelli, L. Botti, B. Ene-Iordache, A. Remuzzi, and D. Steinman, “An image-based modeling framework for patient-specific computational hemodynamics,” *Medical and Biological Engineering and Computing*, vol. 46, pp. 1097–1112, 2008.
- [35] L. Formaggia, A. Quarteroni, and A. Veneziani, Eds., *Cardiovascular Mathematics: Modeling and Simulation of the Circulatory System*, ser. Modeling, Simulation and Applications. Milan: Springer, 2009, vol. 1.
- [36] P. Crosetto, P. Reymond, S. Deparis, D. Kontaxakis, N. Stergiopoulos, and A. Quarteroni, “Fluid-structure interaction simulation of aortic blood flow,” *Computers & Fluids*, vol. 43, no. 1, pp. 46 – 57, 2011.
- [37] E. Marchandise, P. Crosetto, C. Geuzaine, J.-F. Remacle, and E. Sauvage, “Quality open source mesh generation for cardiovascular flow simulations,” in *Modelling Physiological Flow*, ser. Springer Series on Modeling, Simulation and Applications, D. Ambrosi, A. Quarteroni, and G. Rozza, Eds. Springer-Verlag, 2011.
- [38] L. Formaggia, J.-F. Gerbeau, F. Nobile, and A. Quarteroni, “Numerical treatment of defective boundary conditions for the navier-stokes equations,” *SIAM J. Numer. Anal.*, vol. 40, no. 1, pp. 376–401, 2002.

- [39] —, “On the coupling of 3D and 1D Navier–Stokes equations for flow problems in compliant vessels,” vol. 191, no. 6–7, pp. 561–582, 2001.
- [40] A. Veneziani and C. Vergara, “An approximate method for solving incompressible Navier–Stokes problems with flow rate conditions,” vol. 196, no. 9–12, pp. 1685–1700, 2007.
- [41] P. J. Blanco, R. A. Feijóo, and S. A. Urquiza, “A unified variational approach for coupling 3D–1D models and its blood flow applications,” vol. 196, no. 41–44, pp. 4391–4410, 2007.
- [42] A. C. I. Malossi, P. J. Blanco, S. Deparis, and A. Quarteroni, “Algorithms for the partitioned solution of weakly coupled fluid models for cardiovascular flows,” vol. 27, no. 12, pp. 2035–2057, 2011.
- [43] P. Crosetto, S. Deparis, G. Fourestey, and A. Quarteroni, “Parallel algorithms for fluid-structure interaction problems in haemodynamics,” *SIAM Journal of Scientific Computing*, vol. 33, no. 4, pp. 1598–1622, 2011.
- [44] E. Burman, M. A. Fernández, and P. Hansbo, “Continuous interior penalty finite element method for Oseen’s equations,” vol. 44, no. 3, pp. 1248–1274, 2006.
- [45] G. Langewouters, “Visco-elasticity of the human aorta in vitro in relation to pressure and age,” Ph.D. dissertation, Free University, Amsterdam, 1982.
- [46] A. C. I. Malossi, P. J. Blanco, P. Crosetto, S. Deparis, and A. Quarteroni, “Implicit coupling of one-dimensional and three-dimensional blood-flow models with compliant vessels,” 2012, submitted.

MOX Technical Reports, last issues

Dipartimento di Matematica “F. Brioschi”,
Politecnico di Milano, Via Bonardi 9 - 20133 Milano (Italy)

- 11/2012 BONNEMAIN, J.; FAGGIANO, E.; QUARTERONI A.; DEPARIS S.
A Patient-Specific Framework for the Analysis of the Haemodynamics in Patients with Ventricular Assist Device
- 10/2012 LASSILA, T.; MANZONI, A.; QUARTERONI, A.; ROZZA, G.
Boundary control and shape optimization for the robust design of bypass anastomoses under uncertainty
- 09/2012 MAURI, L.; PEROTTO, S.; VENEZIANI, A.
Adaptive geometrical multiscale modeling for hydrodynamic problems
- 08/2012 SANGALLI, L.M.; RAMSAY, J.O.; RAMSAY, T.O.
Spatial Spline Regression Models
- 07/2012 PEROTTO, S; ZILIO, A.
Hierarchical model reduction: three different approaches
- 06/2012 MICHELETTI, S.; PEROTTO, S.
Anisotropic recovery-based a posteriori error estimators for advection-diffusion-reaction problems
- 05/2012 AMBROSI, D; ARIOLI, G; KOCH, H.
A homoclinic solution for excitation waves on a contractile substratum
- 04/2012 TUMOLO, G.; BONAVENTURA, L.; RESTELLI, M.
A semi-implicit, semi-Lagrangian, p-adaptive Discontinuous Galerkin method for the shallow water equations
- 03/2012 FUMAGALLI, A.; SCOTTI, A.
A reduced model for flow and transport in fractured porous media with non-matching grids
- 02/2012 ARIOLI, G.
Optimization of the forcing term for the solution of two point boundary value problems